Opto-Electronic Science

CN 51–1800/O4 ISSN 2097–0382 (Print) ISSN 2097–4000 (Online)

Three-dimensional multichannel waveguide grating filters

Si-Yu Yin, Qi Guo, Shan-Ren Liu, Ju-Wei He, Yong-Sen Yu, Zhen-Nan Tian and Qi-Dai Chen

Citation: Yin SY, Guo Q, Liu SR, et al. Three-dimensional multichannel waveguide grating filters. *Opto-Electron Sci* **3**, 240003 (2024).

https://doi.org/10.29026/oes.2024.240003

Received: 23 January 2024; Accepted: 26 March 2024; Published online: 14 August 2024

Related articles

Opto-Electronic Science

Article

December 2024, Vol. 3, No. 12

DOI: 10.29026/oes.2024.240003

Three-dimensional multichannel waveguide grating filters

Si-Yu Yin, Qi Guo, Shan-Ren Liu, Ju-Wei He, Yong-Sen Yu, Zhen-Nan Tian* and Qi-Dai Chen*

Distributed fiber gratings exhibit outstanding capabilities in achieving a wide spectral response through the superimposition of gratings with different periods in the fiber core. This significantly broadens the design flexibility and potential applications of fiber gratings. However, as photons pass through gratings with varying periods in sequence, which not only inevitably existing signal crosstalk but also poses challenges for integrating. In this study, a three-dimensional (3D) four-channel filter is proposed and realized in fiber-compatible materials using femtosecond laser writing. The filter consists of a 3D beam splitter and four parallel different-period Bragg waveguide gratings (WGs). By designing grating periods in each path, parallel filtering and reflection at multiple designed wavelengths are achieved compactly with 50 nm spectrum spacing within 1450–1600 nm wavelengths. The four-channel filter entire measures 15.5 mm × 1 mm × 1 mm (the highest integration of distributed fiber gratings reported so far). Our technique will augment the laser fabrication technology for 3D integrated photonic devices and serve as a powerful and generalized solution for highly integrated in-situ measurement and multi-parameter decoupled sensing.

Keywords: fiber Bragg grating; waveguide grating filter; three-dimensional; multichannel; femtosecond laser direct-writing

Yin SY, Guo Q, Liu SR et al. Three-dimensional multichannel waveguide grating filters. *Opto-Electron Sci* **3**, 240003 (2024).

Introduction

Fiber Bragg gratings (FBGs) are optical wavelength-sensitive devices formed by periodic refractive index modulation within the core of an optical fiber[1–6]. The strength of the counter-propagating coupling between incident and reflected waves in the device is closely related to the structure of the fiber grating[7–9]. Only light waves that satisfy the Bragg reflection condition can be reflected, giving the device excellent wavelength-selective properties[10]. Furthermore, the device exhibits excellent response characteristics to environmental changes in terms of refractive index and period. The center wavelength of the device's reflected spectrum can vary with the environment[11]. By testing its reflected spectrum, information about environmental factors like temperature, stress, and refractive index can be extracted. Therefore, based on the wavelength-selective and environmentally responsive properties of FBGs, fiber gratings were widely applied in many fields such as filtering, communication, and sensing[12–20]. The center wavelength of the reflected spectrum is determined by the grating period and grating order, typically resulting in a single reflection peak within a bandwidth spanning several hundred nanometers.

In order to simultaneously reflect multiple discrete wavelengths and improve communication filtering and multi-parameter sensing capabilities, distributed fiber optic gratings are essential[21–23]. These gratings are constructed by cascading multiple sub-gratings with different periods in the longitudinal direction. In 2010,

State Key Laboratory of Integrated Optoelectronics, College of Electronic Science and Engineering, Jilin University, Changchun 130012, China.
*Correspondence: ZN Tian, E-mail: zhennan_tian@jlu.edu.cn; QD Chen, E-mail: chenqd@jlu.edu.cn
Received: 23 January 2024; Accepted: 26 March 2024; Published online: 14 August 2024

Graham D. Marshall used a laser point-by-point writing method to fabricate a series of fiber gratings with complex transmission and reflection spectra. This demonstration showcased the versatility and advantages of laser point-by-point writing in creating various complex grating structures[24]. In 2021, Professor Yi-Ping Wang fabricated distributed fiber optic gratings composed of Bragg gratings (BGs) within sapphire optical fibers and researched on their reflection spectrum properties and high-temperature response characteristics[25]. In the same year, Professor Peng-Fei Wang fabricated an ultra-compact fiber grating and a Mach-Zehnder interferometer within optical fibers, enabling simultaneous measurements of strain and temperature[26]. The multi-wavelength reflection and broad spectral response advantages of distributed fiber optic gratings significantly expand the design flexibility and application range of fiber grating devices[27–32].

However, in distributed fiber optic gratings, as photons sequentially pass through sub-grating structures with varying periods, multiple reflections of light can lead to severe crosstalk[33]. Additionally, integrating multiple gratings at different longitudinal positions on the same optical fiber reduces the longitudinal integration density of the device. The sub-gratings are situated at different longitudinal positions within the optical fiber. This inevitably increases the spacing between the gratings, resulting in a reduced spatial resolution for multi-parameter in-situ sensing. Achieving parallel filtering and sensing across multiple channels via integrating multiple sub-gratings in parallel is a promising strategy to enhancing the performance of grating devices. In recent years, femtosecond laser technology has been able to analyze and achieve high-quality 3D structures within novel materials[34–36], playing a crucial role in characterization and manipulation in the micro-world. Moreover, optical waveguide devices manufactured with this technique has found a wide range of applications in both classical and quantum information[37–41]. Femtosecond laser direct writing is a vital technical solution for achieving the lateral 3D integration of multiple sub-gratings[42–46].

In this study, femtosecond laser direct-writing technology was leveraged to achieve one-step fabrication of a multi-channel 3D filter based on BGs with different periods within fused quartz material. This filter is composed of a 3D waveguide optical beam splitter and parallel arrayed BGs that are cascaded on the same chip. After passing through the 3D optical beam splitter, the light is evenly divided into four spatially parallel beams and is individually transmitted to BG structures with different periods that are in-situ integrated using femtosecond laser technology. Parallel filtering and reflection within the wavelength range from 1450 to 1600 nm were achieved on a 15.5 mm × 1 mm × 1 mm chip, with four center wavelengths spaced at 50 nm intervals and a 3-dB bandwidth of approximately 0.37 nm. All waveguide gratings (WGs) in the filter had a length of 6 mm and were arranged at the vertices of a square with a side length of 127 μm, demonstrating excellent compact integration characteristics and obvious powerful scalability. Our technique will augment the laser fabrication technology for 3D integrated photonic devices and serve as a powerful and generalized solution for highly integrated in-situ measurement and multi-parameter decoupled sensing.

Experimental setup

The 3D waveguide beam splitter and BGs with varying periods, forming the 3D multichannel filters, were created within fused quartz. This was achieved through continuous scanning and point-by-point exposure using a 515 nm femtosecond laser. A schematic diagram of the 3D integrated multichannel WGs filters is shown in Fig. 1. The femtosecond laser, with a pulse width of 290 fs, was focused onto a position 170 μm below the surface of the fused quartz, using an objective with a numerical aperture (NA) of 0.55. The laser operated at a repetition rate of 500 kHz. A wide-band single-mode optical fiber was connected on the left side of the filter to input wide-band light into the filter and collect the reflected light. After the reflection by gratings with varying periods, four different wavelength reflection peaks will re-enter the optical fiber.

The fused quartz was affixed on a 3D air-bearing linear displacement stage, which continuously scanned to create the 3D optical waveguides at a speed of 0.3 mm/s. The power of the femtosecond laser was 150 mW, detected before the objective lens. The 3D waveguide beam splitter is composed of two-level directional couplers (DCs). The first-level splitter was arranged in a planar layout, as shown in Fig. 1(a). With coupling length and coupling distance of 0.52 mm and 6 μm, the DC achieved 0.5 : 0.5 beam split. The second-level splitter consisted of two spatially arranged DCs, as shown in Fig. 1(b). With coupling length and coupling distance of 0.63 mm and 6 μm, the splitters achieved a 0.25 : 0.25 : 0.25 : 0.25 beam

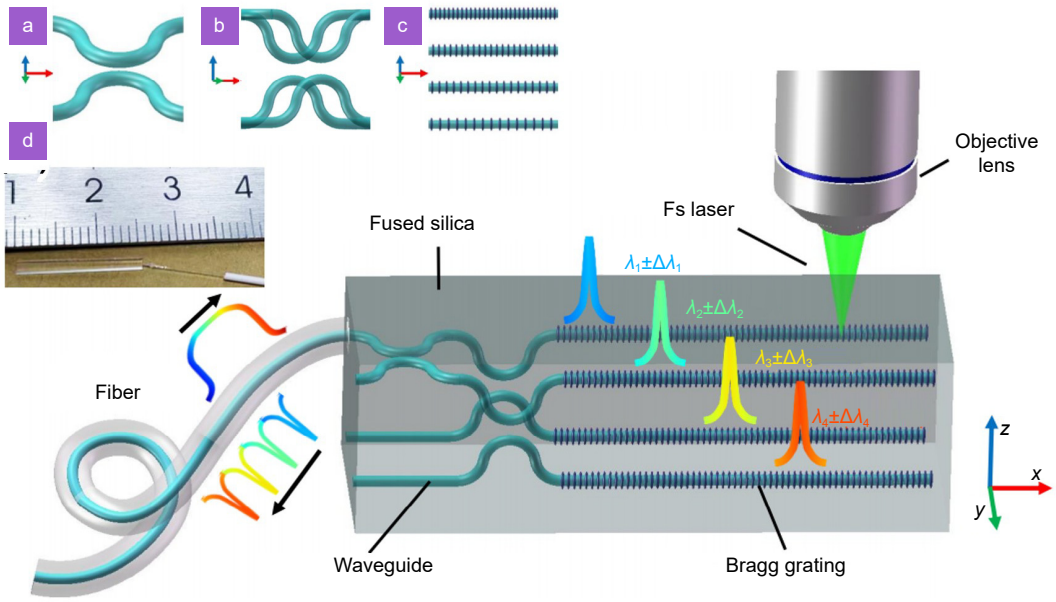

Fig. 1 | Schematic diagram of a 3D integrated multichannel WG filter: (**a**) 1:1 planar beam splitter. (**b**) 1:1 3D beam splitter. (**c**) WGs arranged in parallel with different periods. (**d**) Schematic of the filter attached to the ruler.

split of incident light. All DCs' splitting performance was tested using a 1550 nm laser. By integrating the mode overlap of fiber and waveguide, calculating Fresnel loss (0.29 dB), and testing the insertion loss (5.67 dB), we can obtain the coupling loss (1.25 dB) and propagation loss (0.22 dB/cm), respectively. The bending loss was 1.31 dB/cm with a radius of 40 mm at the bending part of DCs.

BGs are formed in situ on waveguides through point-by-point exposure, as shown in Fig. 1(c). Different exposure times and laser powers of femtosecond pulses create refractive index modulation regions on the original waveguide, resulting in the periodic refractive index distribution of the WG. In the experiments, point-by-point exposure times varied from 0.5 ms to 20 ms, and laser powers ranged from 50 mW to 450 mW. One end of the wideband single-mode optical fiber is encapsulated with the input port of the first-level directional coupler of the filter, while the other end is connected to a supercontinuum light source and a spectrometer through an optical fiber splitter. A physical photograph of the multi-channel filter integrated with optical fiber encapsulation is shown in Fig. 1(d). The overall dimensions of the device are 15.5 mm in length, and both the width and thickness are 1 mm. Within the BGs, coupling occurs between forward and backward propagation modes, and only light that satisfies the Bragg resonance condition will be reflected. The reflection equation is as follows

$$m\lambda = 2n\Lambda\ , \tag{1}$$

where m denotes the grating order, Λ denotes the grating period, n denotes the effective refractive index of the core layer of the waveguide, and λ denotes the wavelength of reflection that generates resonance.

The incident light is divided into four beams after passing through the 3D waveguide beam splitter, and each of them reaches different periodic WG unit filters arranged in parallel. These filters generate reflected light with λ as the central wavelength. Multiple reflected lights with different wavelengths pass through the 3D waveguide beam splitter again, are collected by a wide-band single-mode optical fiber, and enter the spectrometer. The WGs with different periods are arranged in parallel at the vertex positions of a square with a side length of 127 μm and a center distance of 170 μm from the upper surface. Filters based on parallel WGs offer the advantage of compact 3D integration and overcome the issues of reduced signal-to-noise ratio and limited bandwidth caused by the light signal passing through gratings with different periods multiple times. A microscope image of the polished waveguide end faces, mode field energy distribution diagram, and transverse and longitudinal mode energy extraction curves are shown in Fig. 2. The energy distribution of the light-mode field in a four-beam splitter offers valuable insights into how light is distributed within the device, as illustrated in Fig. 2(b). The transverse and longitudinal strength extraction curves for the

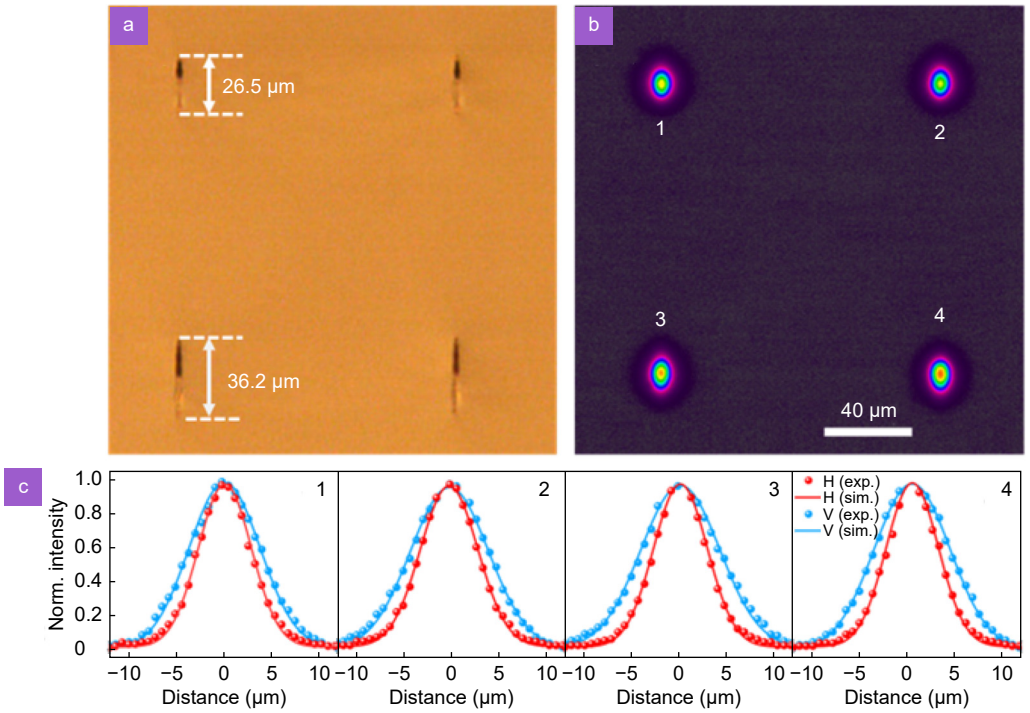

Fig. 2 | Images of the 3D waveguide beam splitter cross-section under a microscope, mode energy distribution map, and mode energy extraction curve. (**a**) Microscope image of the polished cross-section of the waveguide splitter with four waveguides. (**b**) Energy distribution map of the optical mode field for the one-to-four beam splitter. (**c**) Lateral and longitudinal intensity extraction curves of the mode field in figure (b).

mode field represented in Fig. 2(b) are shown in Fig. 2(c). These curves provide additional details about the extraction and distribution of the mode field energy.

In the experiment, varying device coupling spacings and coupling lengths were used to ensure the uniformity of the 3D waveguide beam splitter. Figure 2(a) shows microscopic images of the polished couplers with four output waveguide cross-sections. From the image, it can be observed that the upper half of the cross-section is black, while the lower half is white. The black region represents a damaged area caused by the direct action of the femtosecond laser, resulting in a lower refractive index. The brighter lower part represents a densified region of the material, serving as the core layer of the waveguide, which can confine light[47,48]. The cross-sections of waveguides at the same depth are consistent. The lateral width of the waveguide cross-sections at different depths remains relatively unchanged, approximately 4 μm. However, there is a noticeable difference in the longitudinal dimension of waveguide cross-sections at different depths, where the longitudinal size gradually increases with increasing waveguide depth. For instance, the upper layer waveguide with depth of 106.5 μm has a length of 26.5 μm, while the lower layer waveguide with depth of 233.5 μm has a length of 36.2 μm. This is due to the elliptical energy distribution of the laser within the focal region, which exhibits an elongated ellipsoidal shape along the optical axis. The cross-sectional size of the ellipsoid is determined by the numerical aperture of the objective and remains constant at different depths. However, the length of the ellipsoid increases with depth due to the focusing effect.

The 3D one-to-four beam splitter was characterized with a 1550 nm semiconductor laser. The laser was input into the splitter's input port with a fiber, and the optical energy distribution at the output port is shown in Fig. 2(b). Notably, there was no discernible disparity in the light energy distribution among the four ports. The optical power at the four ports was measured with an optical power meter and recorded as 1.108, 1.005, 1.122, and 1.149 mW, respectively. The sum of the energies at ports 1 and 3, and 2 and 4, which are determined by the first-level splitter, are 2.23 and 2.154 mW, respectively. Thus, the first-level splitting ratio is 0.51 : 0.49. Based on the energy ratios of ports 1 and 3, as well as ports 2 and 4, the splitting ratios of the second-level splitter are obtained as 0.50 : 0.50 and 0.47 : 0.53, respectively. Furthermore, the intensity profiles of the four waveguides in the 3D beam splitter were extracted and shown in Fig. 2(c). The data points extracted from the images in the lateral

and longitudinal directions are marked with red and blue spheres, and the curves obtained by Gaussian fitting of the data points are plotted in corresponding colors. It can be observed that the mode fields have an elliptical shape. The lateral and longitudinal widths of the mode fields for waveguides 1 to 4 are 6.59, 7.15, 6.48, 6.48 μm, and 8.83, 9.67, 9.42, 9.42 μm, respectively. The mode field dimensions for waveguides at different depths do not exhibit significant variations. The fabrication of the 3D uniform beam splitter and compact integrated parallel waveguides forms the foundation for the point-by-point inscription of the multi-channel WG.

The characteristics of the grating are significantly affected by the point-by-point characterization parameters of the WG. In this experimental setup, the laser's single-pulse energy and point-by-point exposure time were controlled. The femtosecond laser was precisely focused at a depth of 170 μm within the material, with single-pulse energy ranging from 300 to 540 nJ and exposure time varying from 1 to 100 ms. An optical microscopic image after point-by-point laser exposure is shown in Fig. 3(a). The laser used for exposure was vertically polarized. The image revealed that the exposure point developed a circular shape with excellent symmetry and lacked any apparent polarization dependence. In addition, it exhibited a ring-like structure with a darker central region and lighter periphery, which was consistent with Fig. 2(a) where the upper end of the waveguide appeared darker while the lower portion was brighter. This may be due to the defocused state of the bright material densification area when inspecting the sparse area at the upper end of the waveguide with a microscope, which was influenced by the depth of the field of the objective lens.

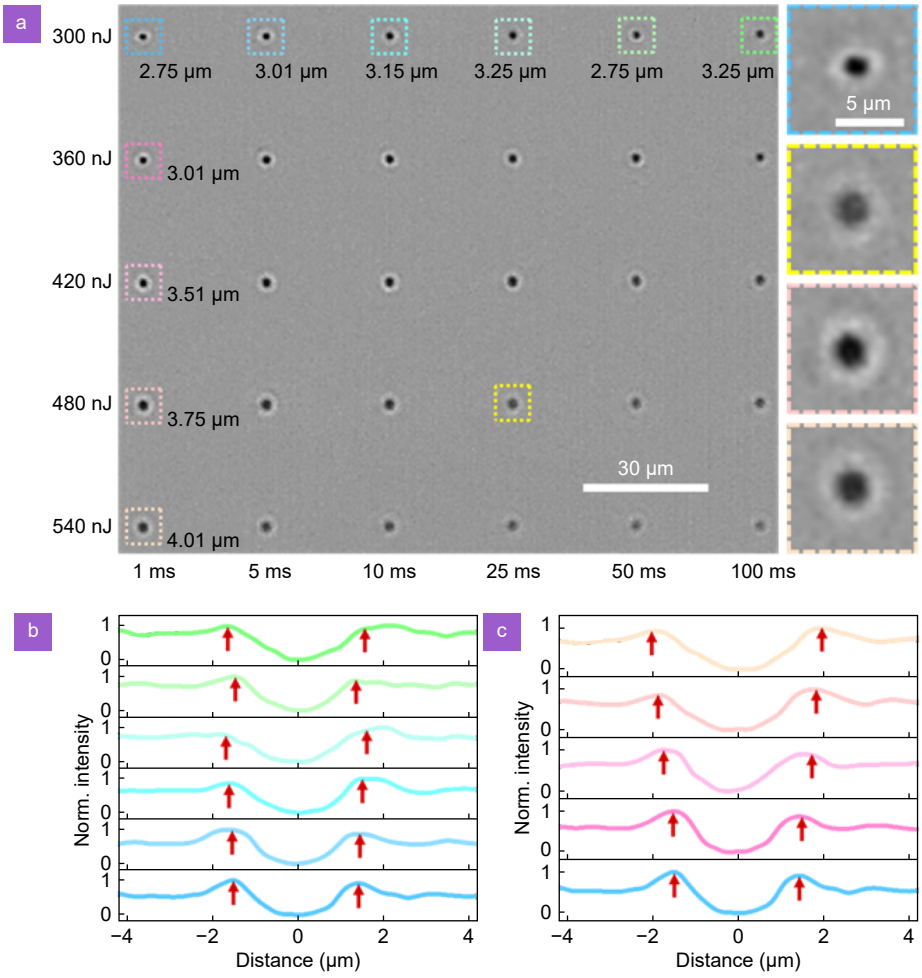

Fig. 3 | Relationships between different laser exposure parameters and exposure point sizes. (**a**) Optical microscope images are shown after single-point exposure with varying laser single-pulse energy and exposure time at a depth of 170 μm inside the material. (**b**) The extracted exposure spot profiles are plotted concerning the change in laser exposure time. (**c**) The extracted exposure spot profiles are plotted concerning the change in laser single-pulse energy.

The relationships between the exposure point topographies and changes in the laser exposure time and single-pulse energy provided further insight, as shown in Fig. 3(b) and 3(c). In Fig. 3(b), the curves of different colors from bottom to top represent the exposure point topography extraction curves with a single-pulse energy of 300 nJ and laser exposure times ranging from 1 ms to 100 ms. In Fig. 3(c), the curves, also of varying colors from bottom to top, depict the exposure point topography extraction curves with a laser exposure time of 1 ms and a single-pulse energy ranging from 300 to 540 nJ. The spacing indicated by the red arrows in the figure was used to determine the diameter of the exposure points. Subsequently, the sizes of the exposure points in the first row and first column of Fig. 3(a) were labeled using black text, and the exposure points for different exposure parameters were outlined with dashed boxes of different colors. From the curves, it is evident that the diameter of the exposure points does not significantly change with increasing exposure time. With the increase in single-pulse energy, the diameter of the exposure points gradually increases from 2.75 μm to 4.01 μm.

Additionally, the exposure point images generated with four sets of parameters were enlarged, encompassing an exposure time of 1 ms and single-pulse energies of 300, 480, and 540 nJ, as well as an exposure time of 25 ms and single-pulse energy of 480 nJ. These images are arranged vertically on the right side of Fig. 3(a). Changes in spot size were aligned with the previously described rules. Given the smaller diameter of the exposure spot with a single-pulse energy of 300 nJ, this value was chosen when investigating the impact of the exposure time and grating order on the WG reflection spectrum. Moreover, an exposure time of 1 ms was selected when examining the influence of the laser power and grating order on the WG reflection spectrum because the exposure time exhibited negligible effects on the exposure point size. Next, we utilized these four sets of parameters to fabricate WGs and characterized the grating period using the Fourier transform method. The characterization

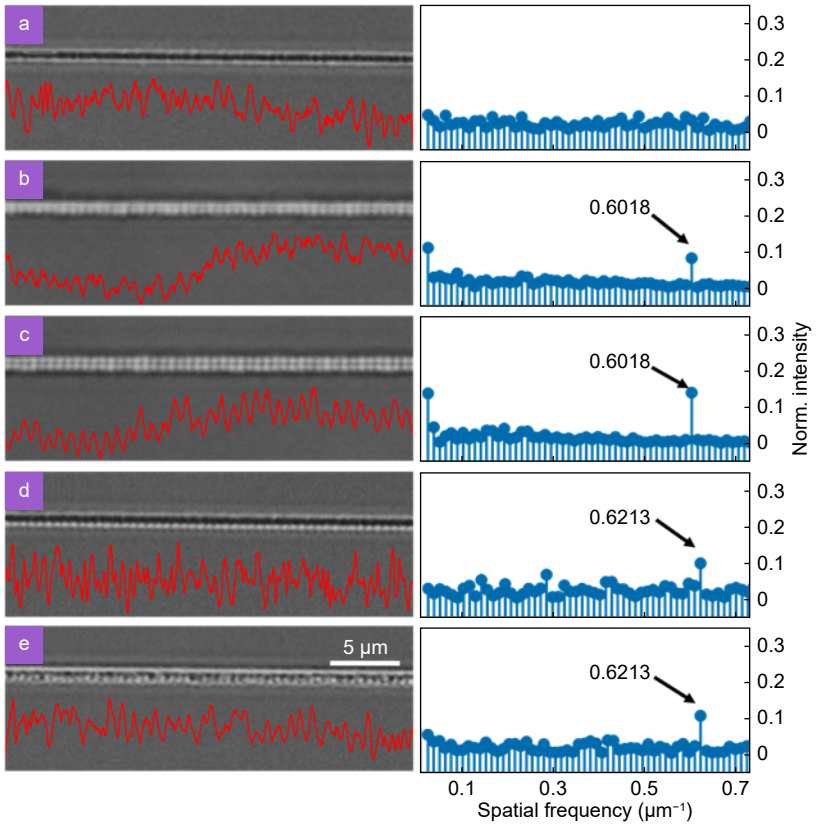

Fig. 4 | Optical microscope images of the WG under various laser writing conditions, intensity extraction curves of the grating images, and the Fourier transform frequency spectrum curves of the intensity curves. The red lines on the left depict a partial microscopic view of the WG and its intensity extraction curve. The blue lines on the right depict the spectrum curve after performing a Fourier transformation on the intensity curve. (**a**) Single straight waveguide without grating. (**b**) Third-order grating with single-pulse energy of 480 nJ and exposure time of 1 ms. (**c**) Third-order grating with single-pulse energy of 480 nJ and exposure time of 25 ms. (**d**) Third-order grating with single-pulse energy of 300 nJ and exposure time of 1 ms. (**e**) Third-order grating with single-pulse energy of 540 nJ and exposure time of 1 ms.

of the WGs under various preparation conditions is shown in Fig. 4.

The four sets of laser parameters shown in Fig. 3 were employed to fabricate the WG structure. The Fourier transform method was utilized to evaluate the periodic characteristics of the gratings. The waveguide within the WG was prepared in fused quartz at a depth of 170 μm, utilizing a scanning speed of 0.3 mm/s and femtosecond laser single-pulse energy of 300 nJ. Figure 4 presents the characterization of WGs fabricated under different conditions. Local microscope images of the WGs and their intensity extraction curves are shown as marked with a red line in the images. The Fourier transform spectrum curves of the intensity profiles are represented by the blue lines on the right. A pure straight waveguide without grating is shown in Fig. 4(a). The intensity curve did not exhibit a refractive-index modulation period, and the Fourier transform spectral curve lacked discernible spatial frequencies. Grating designs with a period of 1.66 μm (constituting a third-order WG with a target wavelength of 1600 nm) for grating direct writing that employed a single-pulse energy of 480 nJ and exposure times of 1 and 25 ms are shown in Fig. 4(b) and 4(c), respectively. Notably, the corresponding spectrum diagram demonstrated evident periodicity with a spatial frequency of 0.6018 μm^{-1}. Similarly, grating designs with a period of 1.61 μm (forming a third-order WG with a target wavelength of 1550 nm) for grating direct writing that utilized an exposure time of 1 ms and single-pulse energies of 300 and 540 nJ are shown in Fig. 4(d) and 4(e), respectively. The corresponding spectral diagram illustrates that the spatial frequency of the WG under different single-pulse energies was 0.6213 μm^{-1}. The calculations determined that the arrows pointing to 0.6018 and 0.6213 on the spectrum curve corresponded to WG periods of 1.662 and 1.610 μm, respectively. These values aligned with the experimentally designed period, substantiating that the single-point exposure time and laser-pulse energy exhibited minimal impacts on the grating periodicity. The reflectivity and 3-dB bandwidth of the WGs were studied with a focus on their optical properties, taking into account exposure time, single-point pulse energy, and grating order.

Theoretical analysis

The reflectivity for a grating with a specific modulation period can be expressed as[24]:

$$R(l,\lambda) = \frac{\Omega^2 \sinh^2(sl)}{\Delta k^2 \sinh^2(sl) + s^2 \cosh^2(sl)}, \tag{2}$$

where R represents the reflectivity function, which depends on length and wavelength. Ω denotes the coupling coefficient, Δk denotes the detuning vector, k represents the propagation constant, and l signifies the grating length. Additionally, s^2 is defined as $\Omega^2 - \Delta k^2$.

The expressions for the reflectivity and width of the resonance line of the grating simplify when there is no detuning in the wave vector at the central wavelength of the Bragg WG ($\Delta k = 0$), and are respectively expressed as

$$R(l,\lambda) = \tanh^2(\Omega l), \tag{3}$$

$$\Delta\lambda = \frac{\lambda^2}{2n}\sqrt{\frac{\Omega^2}{\pi^2} + \frac{1}{l^2}}, \tag{4}$$

$$\Omega = \frac{\pi \Delta n}{\lambda}. \tag{5}$$

Equations (3) to (5) show that the reflectivity and bandwidth of the BG reflection spectrum line are jointly determined by the refractive-index modulation (Δn) and grating length (l). The grating's bandwidth was inversely proportional to its length and had minimal dependence on Ω when $\Omega l < 1$, resulting in a grating reflectivity of less than 58%. This implied that longer gratings tended to exhibit narrower linewidths. Conversely, the grating's bandwidth demonstrated an approximate linear relationship with Ω and was nearly independent of l when $\Omega l > 10$, resulting in a grating reflectivity exceeding 99.99%. Hence, the grating's bandwidth was effectively decreased by reducing Ω. The coupling coefficient Ω can be reduced in point-by-point WG experiments involving laser writing by lowering the laser-pulse energy or increasing the grating order (m), which consequently decreases the grating's bandwidth. While ensuring a smaller bandwidth, it's possible to maintain a constant value of Ωl by increasing the grating's length, thus ensuring higher reflectivity.

An in-depth exploration of the influence of single-point exposure time, laser-pulse energy, and grating order on the optical properties of the gratings was conducted. The collection of reflection spectrum of a third-order WG under different single-point exposure times, each with a laser-pulse energy of 300 nJ, is shown in Fig. S1, Supplementary information. The variation in the reflectivity and 3-dB bandwidth of the waveguide array grating with respect to the single-point exposure time is shown in Fig. 5(a). It is evident that the reflectance and

bandwidth of the spectrum remained relatively stable as the exposure time increased. This observation is consistent with the findings presented in Fig. 3. The collection of reflection spectrum of a third-order WG under various laser-pulse energies while maintaining a single-point exposure time of 1 ms is shown in Fig. S2, Supplementary information. The alteration in the reflectivity and 3-dB bandwidth of the waveguide array grating in response to the laser-pulse energies is shown in Fig. 5(b). Notably, an upward trend was observed in the reflectance and 3-dB bandwidth as the laser-pulse energy increased. This effect was attributed to the augmentation of the grating coupling coefficient Ω with higher laser-pulse energies. According to Eqs. (3) and (4), the reflectivity and bandwidth were positively influenced and increased correspondingly. The collection of reflection spectrum under a single-point exposure time of 1 ms and laser-pulse energy of 300 nJ with varying grating orders is shown in Fig. S3, Supplementary information. The evolution of the reflectivity and 3-dB bandwidth of the waveguide array grating with respect to the grating orders is shown in Fig. 5(c). The reflectance and 3-dB bandwidth exhibited a gradual decrease as the grating order increased. This phenomenon occurred because the number of grating periods decreased with an increase in the grating order at an identical grating length (6 mm). These experimental results were consistent with the earlier discussion of reflectivity and bandwidth formulas.

Results and discussion

Based on the experiment with different laser exposure parameters, the single-point exposure time and laser-pulse energy were selected as 1 ms and 300 nJ to fabricate a four-channel 3D filter. Both experimental and simulation spectra of four-channel 3D filter are shown in Fig. 6. From left to right, the four enlarged views correspond to the reflection spectra at 1450, 1500, 1550, and 1600 nm, whose 3-dB bandwidths are 0.42, 0.34, 0.33, and 0.37 nm, respectively. On the position of peaks in the spectra, the experiment and simulation are in good agreement. As shown in Fig. 6(a), the inconsistency height of the reflection peaks can be attributed to the varying splitting ratios of the beam splitter and different propagation losses at different wavelengths. The 3-dB bandwidths in the experiment were wider than those of the theoretical ones, which was influenced by the uniformity of the gratings resulting from slight deviations of exposure points. Dense periods exposure will increase refractive index of waveguide and decrease the wavelength of reflection peak, which can be corrected by a pre-compensation method.

Through multiple comparative experiments, it has been demonstrated that the single-point exposure time, laser power during the manufacturing process, and the chosen grating order all have an impact on the grating properties. Certainly, this affirms the potential of femtosecond laser direct writing as a precise method for controlling laser exposure parameters and grating-specific characteristics during the manufacturing process. This capability, in turn, enables the production of high-quality BGs inside the medium through point-by-point exposure. By controlling the laser and grating structural parameters, one can manage the amplitude, central wavelength, and bandwidth of the reflection spectra, creating arbitrary reflection and transmission curves. And for the proposed multi-channel parallel waveguide Bragg grating structure, the absence of interference between channels and the prevention of multi-reflection among the gratings effectively eliminate crosstalk. This enables simultaneous multi-channel network information transmission, holding application value in fields such as fiber-to-the-home construction and other optical network transmissions, and is expected to facilitate real-time multi-parameter monitoring of network link status, with promising applications in on-chip all-optical information processing.

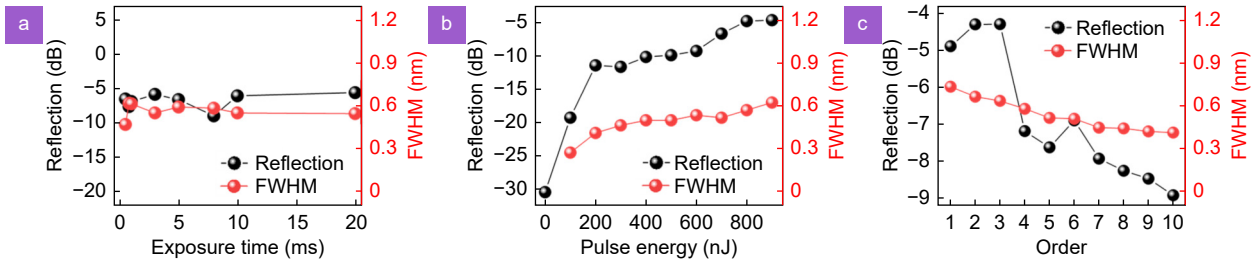

Fig. 5 | Effects of different parameters on the optical properties of the gratings: (**a**) laser exposure time, (**b**) single-pulse energy, and (**c**) grating order on the reflectivity and 3dB-bandwidth of the BG reflection spectrum.

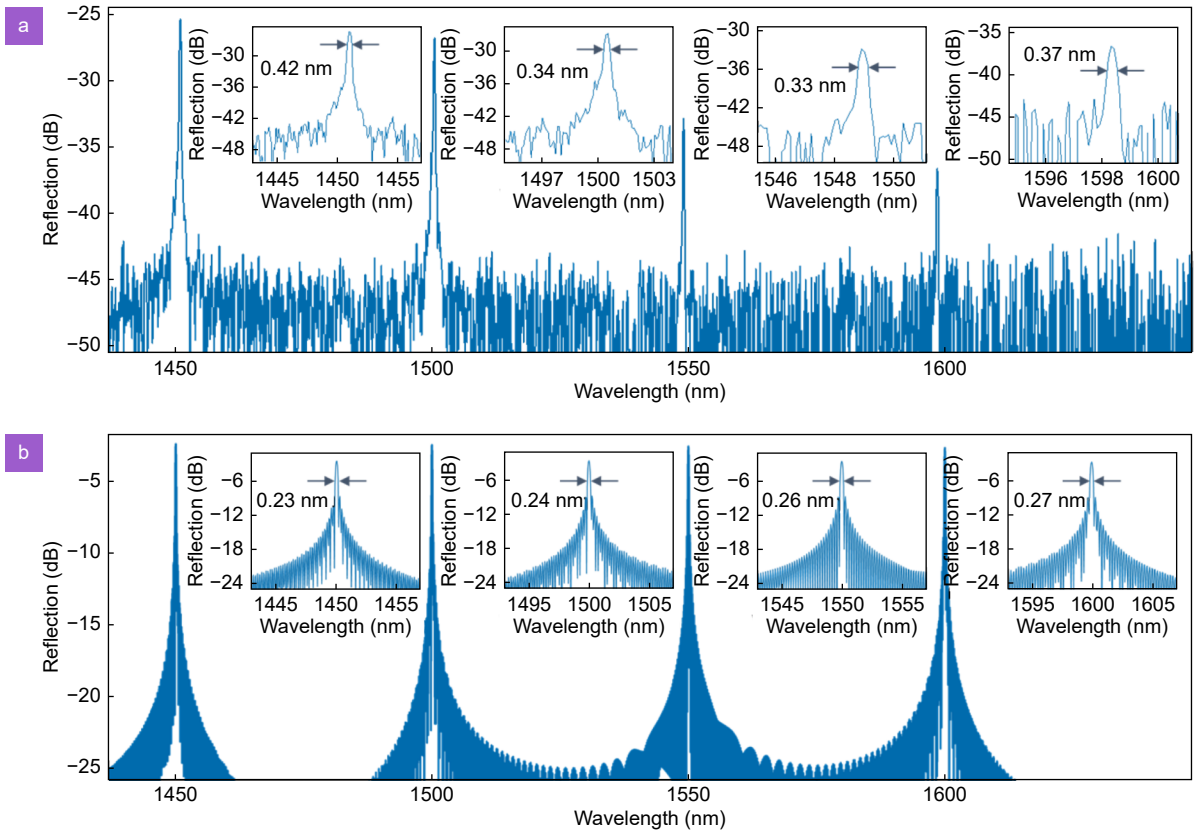

Fig. 6 | Reflectance spectrum of the 3D integrated multi-channel WG filter. (**a**) Experimental and (**b**) Simulation result. The center wavelength of four magnified views was 1450, 1500, 1550, and 1600 nm, respectively.

Conclusions

This study successfully designs and realizes fiber-compatible 3D-integrated multichannel WG filters via femtosecond laser direct-writing technology. The multichannel bandpass filter boasts a straightforward structure, multiple controllable parameters, and ease of scalability. The key parameters affecting the WG performance were theoretically and experimentally verified by investigating the reflection spectrum. A four-channel filter with bandwidths ranging from 1450 nm to 1600 nm and 50 nm intervals was implemented. The four-channel filter entire measures 15.5 mm × 1 mm × 1 mm, which possesses the highest integration of distributed fiber gratings reported so far. Our technique will augment laser fabrication techniques for both classical and quantum 3D integrated photonic devices. The multi-channel parallel strategy will serve as a powerful and versatile solution for highly integrated in-situ measurements and multi-parameter decoupled sensing.

References

1. Kondo Y, Nouchi K, Mitsuyu T et al. Fabrication of long-period fiber gratings by focused irradiation of infrared femtosecond laser pulses. *Opt Lett* **24**, 646–648 (1999).
2. Rao YJ. Recent progress in applications of in-fibre Bragg grating sensors. *Opt Laser Eng* **31**, 297–324 (1999).
3. Liang W, Huang YY, Xu Y et al. Highly sensitive fiber Bragg grating refractive index sensors. *Appl Phys Lett* **86**, 151122 (2005).
4. Mihailov SJ. Fiber Bragg grating sensors for harsh environments. *Sensors* **12**, 1898–1918 (2012).
5. Albert J, Shao LY, Caucheteur C. Tilted fiber Bragg grating sensors. *Laser Photonics Rev* **7**, 83–108 (2013).
6. Li Z, Chen JX, Li LZ et al. Exceptional-point-enhanced sensing in an all-fiber bending sensor. *Opto-Electron Adv* **6**, 230019 (2023).
7. Wolf A, Dostovalov A, Bronnikov K et al. Advances in femtosecond laser direct writing of fiber Bragg gratings in multicore fibers: technology, sensor and laser applications. *Opto-Electron Adv* **5**, 210055 (2022).
8. Lu CG, Cui YP. Fiber Bragg grating spectra in multimode optical fibers. *J Lightwave Technol* **24**, 598–604 (2006).
9. Martins ER, Wang Y, Kanibolotsky AL et al. Low-threshold nanoimprinted lasers using substructured gratings for control of distributed feedback. *Adv Opt Mater* **1**, 563–566 (2013).
10. Helan R, Urban F. Principle of fiber Bragg gratings measurement. In *30th International Spring Seminar on Electronics Technology* 352–356 (IEEE, 2007); http://doi.org/10.1109/isse.2007.4432878.
11. Tosi D. Review of chirped fiber Bragg grating (CFBG) fiber-optic sensors and their applications. *Sensors* **18**, 2147 (2018).

12. Hongo A, Kojima S, Komatsuzaki S. Applications of fiber Bragg grating sensors and high-speed interrogation techniques. *Struct Control Health Monit* **12**, 269–282 (2005).
13. Song DC, Wei ZX, Zou JL et al. Pressure sensor based on fiber Bragg grating and carbon fiber ribbon-wound composite cylindrical shell. *IEEE Sens J* **9**, 828–831 (2009).
14. Liu XM, Han DD, Sun ZP et al. Versatile multi-wavelength ultrafast fiber laser mode-locked by carbon nanotubes. *Sci Rep* **3**, 2718 (2013).
15. Liu HH, Hu DJJ, Sun QZ et al. Specialty optical fibers for advanced sensing applications. *Opto-Electron Sci* **2**, 220025 (2023).
16. Campanella CE, Cuccovillo A, Campanella C et al. Fibre Bragg grating based strain sensors: review of technology and applications. *Sensors* **18**, 3115 (2018).
17. Sun QZ, Li H, Fan CZ et al. Research progress of distributed acoustic sensing based on scattering enhanced optical fiber. *Laser Optoelectron Prog* **59**, 2100001 (2022).
18. Wang H, Tao CY, Gao XF et al. Detection of dynamic strain using an SOA-fiber ring laser and an arrayed waveguide grating demodulator. *Optoelectron Lett* **18**, 331–337 (2022).
19. Rao YJ, Wang YP, Ran ZL et al. Novel fiber-optic sensors based on long-period fiber gratings written by high-frequency CO_2 laser pulses. *J Lightwave Technol* **21**, 1320–1327 (2003).
20. Jiang BQ, Hou YG, Wu JX et al. In-fiber photoelectric device based on graphene-coated tilted fiber grating. *Opto-Electron Sci* **2**, 230012 (2023).
21. Song KY, Hotate K, Zou WW et al. Applications of Brillouin dynamic grating to distributed fiber sensors. *J Lightwave Technol* **35**, 3268–3280 (2017).
22. Senevirathne CAM, Sandanayaka ASD, Karunathilaka BSB et al. Markedly improved performance of optically pumped organic lasers with two-dimensional distributed-feedback gratings. *ACS Photonics* **8**, 1324–1334 (2021).
23. Chen YS, Mo SY, Li WZ et al. Applications of distributed fiber Bragg gratings to the measurements of in-tube fluid temperature distribution. *Appl Therm Eng* **220**, 119724 (2023).
24. Marshall GD, Williams RJ, Jovanovic N et al. Point-by-point written fiber-Bragg gratings and their application in complex grating designs. *Opt Express* **18**, 19844–19859 (2010).
25. Xu XZ, He J, He J et al. Efficient point-by-point Bragg grating inscription in sapphire fiber using femtosecond laser filaments. *Opt Lett* **46**, 2742–2745 (2021).
26. Tian K, Zhang MY, Zhao ZY et al. Ultra-compact in-core-parallel-written FBG and Mach-Zehnder interferometer for simultaneous measurement of strain and temperature. *Opt Lett* **46**, 5595–5598 (2021).
27. Ashry I, Mao Y, Wang BW et al. A review of distributed fiber-optic sensing in the oil and gas industry. *J Lightwave Technol* **40**, 1407–1431 (2022).
28. Lu P, Mihailov SJ, Coulas D et al. Low-loss random fiber gratings made with an fs-IR laser for distributed fiber sensing. *J Lightwave Technol* **37**, 4697–4702 (2019).
29. Westbrook PS, Kremp T, Feder KS et al. Continuous multicore optical fiber grating arrays for distributed sensing applications. *J Lightwave Technol* **35**, 1248–1252 (2017).
30. Kim HI, Kang LH, Han JH. Shape estimation with distributed fiber Bragg grating sensors for rotating structures. *Smart Mater Struct* **20**, 035011 (2011).
31. Li GL, Wang F, Feng F et al. Hot spot detection of photovoltaic module based on distributed fiber Bragg grating sensor. *Sensors* **22**, 4951 (2022).
32. Guo YM, Ding ZY, Liu K et al. Two-dimensional distributed strain sensing with an Archimedean spiral arrangement in optical frequency domain reflectometry. *Nanotechnol Precis Eng* **1**, 187–190 (2018).
33. Guo HY, Qian L, Zhou CM et al. Crosstalk and ghost gratings in a large-scale weak fiber Bragg grating array. *J Lightwave Technol* **35**, 2032–2036 (2017).
34. Li XK, Sun K, Wu JJ et al. Thermal-triggered phase separation and ion exchange enables photoluminescence tuning of stable mixed-halide perovskite nanocrystals for dynamic display. *Laser Photonics Rev* **18**, 2301244 (2024).
35. Sun K, Zhang B, Gao K et al. Localized temperature engineering enables writing of Heterostructures in glass for polarized photoluminescence of perovskites. *ACS Nano* **18**, 6550–6557 (2024).
36. Qiu LR, Su YH, Xu KM et al. A high-precision multi-dimensional microspectroscopic technique for morphological and properties analysis of cancer cell. *Light Sci Appl* **12**, 129 (2023).
37. Kowalevicz AM, Sharma V, Ippen EP et al. Three-dimensional photonic devices fabricated in glass by use of a femtosecond laser oscillator. *Opt Lett* **30**, 1060–1062 (2005).
38. Pospiech M, Emons M, Väckenstedt B et al. Single-sweep laser writing of 3D-waveguide devices. *Opt Express* **18**, 6994–7001 (2010).
39. Spagnolo N, Aparo L, Vitelli C et al. Quantum interferometry with three-dimensional geometry. *Sci Rep* **2**, 862 (2012).
40. Chaboyer Z, Meany T, Helt LG et al. Tunable quantum interference in a 3D integrated circuit. *Sci Rep* **5**, 9601 (2015).
41. Tang H, Lin XF, Feng Z et al. Experimental two-dimensional quantum walk on a photonic chip. *Sci Adv* **4**, eaat3174 (2018).
42. Martinez A, Dubov M, Khrushchev I et al. Direct writing of fibre Bragg gratings by femtosecond laser. *Electron Lett* **40**, 1170–1172 (2004).
43. Zhang HB, Eaton SM, Li JZ et al. Femtosecond laser direct writing of multiwavelength Bragg grating waveguides in glass. *Opt Lett* **31**, 3495–3497 (2006).
44. Grenier JR, Fernandes LA, Herman PR. Femtosecond laser writing of optical edge filters in fused silica optical waveguides. *Opt Express* **21**, 4493–4502 (2013).
45. Xiong C, Jiang W, Wang CY et al. Fiber Bragg gratings inscribed in nanobore fibers. *Opt Lett* **48**, 2821–2824 (2023).
46. Chen ZY, He J, Xu XZ et al. High-temperature sensor array based on fiber Bragg gratings fabricated by femtosecond laser point-by-point method. *Acta Opt Sinica* **41**, 1306002 (2021).
47. Chan JW, Huser T, Risbud S et al. Structural changes in fused silica after exposure to focused femtosecond laser pulses. *Opt Lett* **26**, 1726–1728 (2001).
48. Streltsov AM, Borrelli NF. Study of femtosecond-laser-written waveguides in glasses. *J Opt Soc Am B* **19**, 2496–2504 (2002).

Acknowledgements

This work was supported in part by the National Natural Science Foundation of China under Grant No. 62375103 and Grant No. 62131018, in part by the National Key Research and Development Program of China under Grant No. 2021YFF0502700, and Innovation Program for Quantum Science and Technology (Grant No. 2021ZD0300701).

Author contributions

S.-Y. Yin, Q. Guo, S.-R. Liu and J.-W. He conducted the experiments and performed data analysis, S.-Y. Yin and Z.-N. Tian wrote the manuscript, Z.-N. Tian and Q. Guo conceived the idea, Q.-D. Chen, Z.-N. Tian, and Y.-S. Yu supervised the work. All the authors discussed and analyzed the results and commented on the manuscript at all stages.

Competing interests

The authors declare no competing financial interests.

Supplementary information

Supplementary information for this paper is available at https://doi.org/10.29026/oes.2024.240003

Scan for Article PDF